Optical Materials 159 (2025) 116580

Contents lists available at ScienceDirect

Optical Materials

journal homepage: www.elsevier.com/locate/optmat

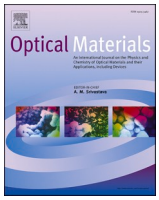

Research Article

Double-phase Nd^{3+}, Yb^{3+}:CeF_3/CeO_2 nanoparticles as potential materials for optical temperature sensing

A.K Ginkel [a,*], R.M Rakhmatullin [a], O.A Morozov [a,b], I.A Zagrai [c], S.L Korableva [a], M.S Pudovkin [a,**]

[a] Kazan Federal University, Institute of Physics, 18 Kremlyovskaya Str, Kazan, 420008, Russia
[b] Zavoisky Physical-Technical Institute, FRC Kazan Scientific Center of RAS, Sibirsky Trakt Str. 10, Kazan, 420029, Russia
[c] Vyatka State University, Kirov, 610000, Russia

ARTICLE INFO

Keywords:
Luminescent thermometry
Optical temperature sensing
Nd^{3+}/Yb^{3+}
CeF_3
CeO_2

ABSTRACT

In this work, we study the possibility the use of Nd^{3+}, Yb^{3+}:CeF_3/CeO_2 nanoparticles in ratiometric luminescence thermometry. In order to explain the mechanism of the luminescence temperature sensitivity, we physically characterized the samples by means of transmission electron microscopy (TEM), X-ray diffraction (XRD), laser spectroscopy, and electron paramagnetic resonance (EPR). In particular, Nd^{3+}, Yb^{3+}:CeF_3 nanoparticles were synthesized via co-precipitation method and annealed in air at 600 °C for 0, 15, 30, 60, and 120 min to obtain double-phase Nd^{3+}, Yb^{3+}:CeF_3/CeO_2 nanoparticles as well as single-phase Nd^{3+}, Yb^{3+}:CeO_2 ones (at 120 min). The physical diameter of the samples gradually increases from 19 ± 2 (doped CeF_3) to 409 ± 18 nm (doped CeO_2). It was suggested, that the double-phase samples consist of sintered doped CeF_3 and CeO_2 nanoparticles having average grain diameter around 65 nm. The single-phase CeO_2 sample also consists of sintered CeO_2 nanoparticles, suggestively. The luminescence intensity ratio (LIR) was analyzed in the 80–320 K range (LIR = I_{Nd}/I_{Yb}, where 848–925 nm ($^4F_{3/2}$ – $^4I_{9/2}$) Nd^{3+} and 925–1048 nm ($^2F_{5/2}$ – $^2F_{7/2}$) Yb^{3+}). The maximal relative temperature sensitivity was achieved for Nd^{3+}, Yb^{3+}:CeO_2 sample (~0.2 %/K), which is very competitive value. The LIR function has a simple linear temperature dependency in the broad 80–320 K which allows uniquely identifying the temperature at least in the studied broad temperature range. The mechanism of temperature sensitivity was suggested.

1. Introduction

Luminescence temperature sensing is a very powerful tool in order to obtain information about the temperature of the studied object with submicron spatial resolution. In addition, this technique allows performing temperature sensing remotely in the depth of the object or from its surface [1–6]. This feature is in demand in cancer hyperthermia, microcircuit manufacturing, dentistry, etc. In particular, this method is required in noninvasive probing and monitoring the temperature during photopolymerization of dental materials [7]. This method allows high spatial resolution temperature mapping in order to determine the stability of microcircuits [8]. In the case of hyperthermia, this method makes it possible to control the temperature of the tumor which is heated is the use of biocompatible luminescence nanoparticles operating in the so-called biological window [9,10]. In turn, the overheating leads to necrosis and the damage of the neighboring healthy tissues. Very promising nanomaterials for the above-mentioned purposes are considered rare-earth doped fluoride nanoparticles. Indeed, due to the low phonon energy [11], high chemical and mechanical stability [12], lack of photobleaching, and low cytotoxicity [13–15], these materials serve as luminescent probes for many scientific, medical, and industrial purposes.

Among a huge variety of rare-earth doped nano- and microparticles, the Nd^{3+}/Yb^{3+} ones are considered very promising for temperature sensing in the "biological window" [16–18]. Here, Nd^{3+} serves as a donor of the energy, and Yb^{3+} serves as an acceptor. In the case of the biological window, Nd^{3+} can be excited at least by ~790 and ~808 nm corresponding to $^4I_{9/2}$ – $^4F_{5/2}$ and $^4I_{9/2}$ – $^4F_{3/2}$ Nd^{3+} absorption bands, respectively. Having excited Nd^{3+} ions, the phonon-assisted energy transfer to Yb^{3+} occurs ($^4F_{3/2}$ (Nd^{3+}) – $^2F_{5/2}$ (Yb^{3+})) [19]. Thus, the

* Corresponding author.
** Corresponding author.
E-mail addresses: anna.dokudovskaya006@mail.ru (A.K Ginkel), maksim.s.pudovkin@gmail.com (M.S Pudovkin).

https://doi.org/10.1016/j.optmat.2024.116580
Received 16 October 2024; Received in revised form 23 November 2024; Accepted 15 December 2024
Available online 16 December 2024

temperature sensitivity of the spectral characteristics is based on the temperature-dependent phonon-assisted energy transfer. Here, the integrated luminescence intensity ratio (LIR) of Nd^{3+} (~900 nm, $^4F_{3/2}$ – $^4I_{9/2}$ transition) and Yb^{3+} (~1000 nm, $^2F_{5/2}$ – $^2F_{7/2}$ transition) is often taken as a temperature-dependent parameter. However, the character of the LIR temperature dependence for different matrices differs from each other. Specifically, the Nd^{3+}/Yb^{3+} ion pair in $LiLaP_4O_{12}$ shows decreasing character in the 100–500 K temperature range [20]. In turn, in our previous works, the LIR demonstrated more complicated character with increasing and decreasing parts. Such interesting LIR behavior probably occurs because of more complex character of energy exchange between Nd^{3+} and Yb^{3+} ions. There are Nd^{3+} - Yb^{3+} energy transfer, Yb^{3+} - Nd^{3+} back energy transfer, energy diffusion between Yb^{3+} ions, and cross-relaxation between Nd^{3+} ions. The cross-relaxation between Nd^{3+} and Yb^{3+} ions is also possible under UV or blue excitation [21]. In the case of "biological window" excitation, this process is not considered. In the work, it was mentioned, that the phonon-assisted energy transfer can occur via $^4F_{5/2}$ (Nd^{3+}) and $^2F_{5/2}$ (Yb^{3+}). The thermal expansion phenomenon which affects the distances between doping ions can also play a notable role [22].

The main problem is, that in some cases, the LIR function shape is complicated, and there are two or\and more LIR values corresponding to a particular temperature value. It leads to the ambiguous definition of temperature. Hence, it is necessary to choose an appropriate host-matrix as well as the concentrations of the doping ions.

Here we considered Nd^{3+}/Yb^{3+} doped CeF_3 nanoparticles annealed in air for different times in order to obtain double-phase Nd^{3+}/Yb^{3+} doped CeF_3/CeO_2 nanoparticles as well as single-phase Nd^{3+}/Yb^{3+} doped CeO_2 ones (at the highest annealing time). The objective of this research is to create a material for optical temperature sensing operating in the "biological window" that is capable of ambiguous definition of temperature (simple LIR function). In addition, we synthesized Nd^{3+}/Yb^{3+} doped CeO_2 nanoparticles via chemical method in order to compare of the thermometric performances of Nd^{3+}/Yb^{3+} doped CeO_2 obtained by different methods.

The tasks were:

- The chemical synthesis of the Nd^{3+}/Yb^{3+} doped CeF_3 and CeO_2 nanoparticles;
- The annealing in air of the synthesized Nd^{3+}/Yb^{3+} doped CeF_3 nanoparticles in order to obtain double-phase Nd^{3+}/Yb^{3+} doped CeF_3/CeO_2 nanoparticles as well as single-phase Nd^{3+}/Yb^{3+} doped CeO_2 ones;
- Physical characterization of the obtained samples via transmission electron microscopy, X-ray diffraction, and Raman spectroscopy;
- Luminescence characterization of the samples;
- Electron paramagnetic resonance characterization of the samples;
- Calculation of the LIR functions, absolute, and relative temperature sensitivities;
- The choice of the appropriate sample for temperature sensing in the "biological window".

The choice of the above-mentioned ceria compounds was based on the fact, that both CeO_2 and CeF_3 demonstrated low cytotoxicity [23]. Both types of nanoparticles showed sufficient antioxidant activity which is very important for biomedical applications [24]. Moreover, CeF_3 showcased the photodynamic activity under X-ray irradiation. All the above-mentioned facts make CeO_2, CeF_3, and their combinations very promising materials as multifunctional nano-platforms for the huge variety of biomedical applications.

2. Materials and methods

2.1. The synthesis of the samples

The Nd^{3+}/Yb^{3+} doped CeF_3 nanoparticles were synthesized via the conventional water-based co-precipitation method. The Ce $(NO_3)_3{\cdot}6H_2O$, $Nd(NO_3)_3{\cdot}6H_2O$, $Yb(NO_3)_3{\cdot}4H_2O$, and NH_4F were taken as starting materials. The nanoparticle synthesis was conducted according to the chemical reaction [25]:

$$Ce(NO_3)_3 + 3NH_4F \rightarrow CeF_3 + 3NH_4NO_3$$

In order to synthesize the double-doped Nd^{3+}(0.1 mol.%), Yb^{3+}(0.5 mol.%):CeF_3 nanoparticles we took $Ce(NO_3)_3{\cdot}6H_2O$ (m = 13.020 g), Nd $(NO_3)_3{\cdot}6H_2O$ (m = 0.013 g), $Yb(NO_3)_3{\cdot}4H_2O$ (0.013 g). The powders were dissolved in 30 ml of distilled water. In turn, 3.33 g of NH_4F was dissolved in 90 g distilled water. Two solutions were mixed and the obtained mixture was placed on the magnetic stirrer for 30 min (400 rpm). The obtained precipitate was purified via centrifugation (eight times, around 10 000 rpm for 10 min) using distilled water. The precipitate was dried in air in the dust-proof chamber.

In order to obtain double-phase CeF_3/CeO_2 samples, the synthesized CeF_3 powder was divided into several 0.37 g portions which were annealed in air into a ceramic crucible for 15, 30, 60, and 120 min at 600 °C using muffle furnace. As in will be revealed belong, the sample annealed for 120 min is single-phase doped CeO_2. We also compared spectral characteristics of this single-phase doped CeO_2 with the Nd^{3+}, Yb^{3+}:CeO_2 nanoparticles synthesized co-precipitation method [26,27].

For the sake of the comparison of the Nd^{3+}, Yb^{3+}: CeO_2 (annealed for 120 min) we also synthesized Nd^{3+}, Yb^{3+}: CeO_2 nanoparticles via co-precipitation method. We also took $Ce(NO_3)_3{\cdot}6H_2O$ (m = 4.992 g), Nd $(NO_3)_3{\cdot}6H_2O$ (m = 0.005 g), $Yb(NO_3)_3{\cdot}4H_2O$ (0.0258 g). The powders were dissolved in 120 ml distilled water. 16.224 g of hexamethylenetetramine were dissolved in 390 ml distilled water. Two solutions were mixed and the obtained mixture was placed on the magnetic stirrer and heated to 60 °C. The solution at 60 °C had been stirred for 12 h. The obtained precipitate was also washed via centrifugation.

Here we consider six samples:

Sample	Composition	Annealing temperature (^{0}C) and annealing time (min.)
1	Nd^{3+} (0.1 mol. %), Yb^{3+} (0.5 mol. %): CeF_3 (synthesized by co-precipitation method)	Annealed at 150 °C in vacuum fot 60 min
2	Nd^{3+} (0.1 mol. %), Yb^{3+} (0.5 mol. %): CeF_3/CeO_2	600 °C annealing in air, 15 min
3	Nd^{3+} (0.1 mol. %), Yb^{3+} (0.5 mol. %): CeF_3/CeO_2	600 °C annealing in air, 30 min
4	Nd^{3+} (0.1 mol. %), Yb^{3+} (0.5 mol. %): CeF_3/CeO_2	600 °C annealing in air, 60 min
5	Nd^{3+} (0.1 mol. %), Yb^{3+} (0.5 mol. %): CeO_2	600 °C annealing in air, 120 min
6	Nd^{3+} (0.1 mol. %), Yb^{3+} (0.5 mol. %): CeO_2 (chemically synthesized by co-precipitation method)	300 °C annealing in vacuum, 60 min

In summary, we studied five samples (1–5) of doped CeF_3 which was annealed in air for 15, 30, 60, and 120 min. For 15, 30, and 60 min, we obtained doped-double phase CeF_3/CeO_2 composites. After the 120 min annealing procedure, we got single-phase doped CeO_2 oxide. We also synthesized doped CeO_2 nanoparticle by a chemical route in order to compare some thermometric performances of both doped CeO_2 obtained by different routes. The physical characterization (TEM and XDR) of the 1–5 samples is presented in the manuscript. The physical characterization of the chemically synthesized doped CeO_2 is presented in the Supplementary file.

The Nd^{3+} (0.1 mol. %) and Yb^{3+} (0.5 mol. %) concentration values were determined via the ratio of the starting materials $Ce(NO_3)_3{\cdot}6H_2O$, $Nd(NO_3)_3{\cdot}6H_2O$, and $Yb(NO_3)_3{\cdot}4H_2O$. Since we consider only one Nd^{3+} (0.1 mol. %) and Yb^{3+} (0.5 mol. %) concentration ratio, we will not specify concentration values in the manuscript. In the case of annealed samples, we will use name:

Nd^{3+} (0.1 mol. %), Yb^{3+} (0.5 mol. %): CeF_3/CeO_2 ("time" of annealing), (time = 15, 30, 60, or 120 min.

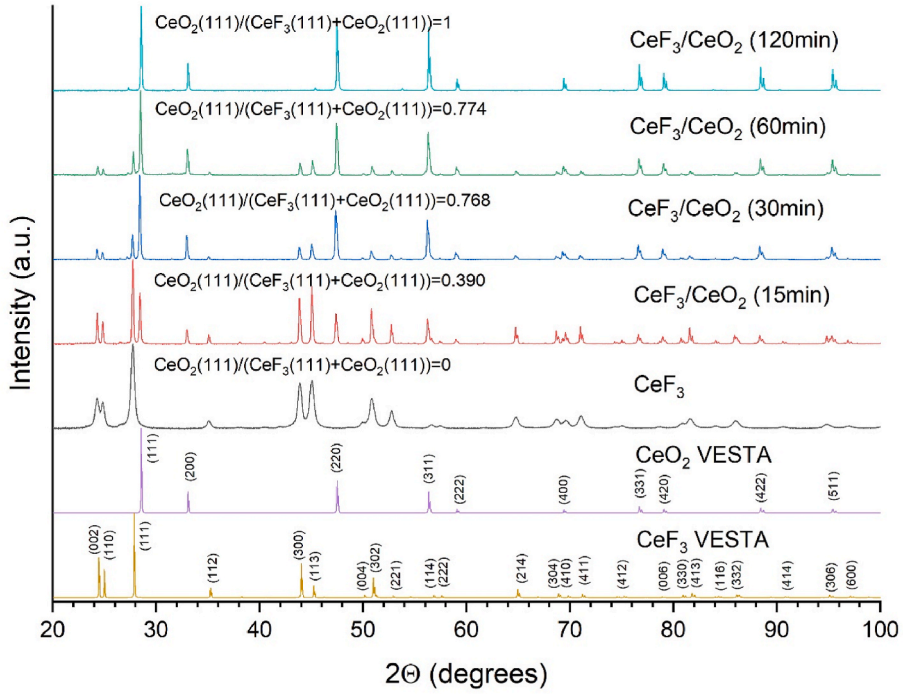

Fig. 1. XRD patterns of the Nd^{3+}, Yb^{3+}:CeF_3 and Nd^{3+}, Yb^{3+}:CeF_3/CeO_2 nanoparticles and the VESTA simulation patterns (in this figure we name the samples without doping ions for brevity's sake).

The chemically synthesized Nd^{3+} (0.1 mol. %), Yb^{3+} (0.5 mol. %): CeF_3/CeO_2 will be called "Nd^{3+}, Yb^{3+}:CeO_2 synthesized via chemical rout"

Not-annealed initial sample will be called Nd^{3+}, Yb^{3+}: CeF_3

2.2. Physical characterization of the samples

The phase compositions of the samples were investigated by an X-ray diffraction method (XRD) using Bruker D8 Advance X-ray diffractometer (Cu K_α radiation $\lambda = 0.154$ nm). The morphology of the samples was studied via transmission electron microscopy (TEM) using Hitachi HT7700 Exalens transmission electron microscope. Luminescence spectra were obtained using a CCD spectrometer (StellarNet) having 0.5 nm spectral resolution. The optical excitation of the luminescence signal was carried out using a laser system based on optical parametric oscillator produced by SP LOTIS 4 ($\lambda_{exc} = 790$ nm corresponds to the $^4I_{9/2}$ - $^4F_{5/2}$ absorption band of Nd^{3+} ion). The pulse duration and pulse repetition rate were 10 ns and 10 Hz, respectively. The spectral width of the laser radiation was less than 0.15 nm. The excitation energy density was less than 10 mJ per 1 cm^2.

The EPR measurements were carried out using continuous wave spectrometer Bruker ESP-300 operating at X-band (~9.4 GHz). The standard modulation frequency was 100 kHz, the modulation amplitude 1–5 G, the typical power level was 25 mW. Low temperatures were obtained with a commercial liquid-helium flow cryostat system (Oxford Instruments).

The spectral characterization was carried out in the 80–320 K temperature range using the "cold finger" method using a CRYO Industries cryostat with a LakeShore Model 325 temperature controller (USA). Liquid nitrogen was used as a cooling agent. The luminescence decay curves were recorded using a BORDO 211 A digital oscilloscope (bandwidth 10 bits, 200 MHz), MDR-3 monochromator, and PEM-62 photomultiplier (operating spectral range ~ 600–1200 nm).

3. Results and discussion

3.1. Physical characterization of the samples via TEM, XRD, and Raman spectroscopy

The XRD spectra of the samples and the VESTA simulations are presented in Fig. 1. Analysis of the XRD spectrum of the CeF_3 nanoparticles (before annealing) demonstrates a hexagonal structure, corresponding to the structure of the CeF_3 host. After the annealing of CeF_3 nanoparticles using the above-mentioned method, a gradual structural-phase transition occurs from the hexagonal phase to the cubic one. The cubic phase corresponds to the structure of CeO_2 host.

In particular, there is a XRD pattern of single-phase Nd^{3+}, Yb^{3+}:CeF_3 nanoparticles which is in good agreement with the VESTA simulation of CeF_3 as well as with the literature data [28,29]. After the 15 min annealing, the peaks corresponding to the CeO_2 phase appear. The intensity of CeO_2 peaks increases with the increase of the annealing time compared to the peaks of the CeF_3 phase. TEM image and size distribution histogram of single-phase Nd^{3+}, Yb^{3+} doped CeO_2 nanoparticles synthesized via the chemical rout are presented in Fig. S1b of the Supplementary file. The average diameter of the obtained nanoparticles is 27 ± 1 nm. According to the XRD data (Fig. S1c) the chemically obtained doped CeO_2 nanoparticles also demonstrate desirable cubic phase corresponding to CeO_2 host.

After 120 min annealing, the sample becomes single-phase one corresponding to the cubic CeO_2 phase. We also compared VESTA simulation with the corresponding JCDS (Fig. S1d of the Supplementary). It can be seen, that they are match together. In particular, CeO_2 corresponds to JCPDS-34-0394. In turn, CeF_3 corresponds to JCPDS-08-0045.

TEM images of Nd^{3+}, Yb^{3+}:CeF_3/CeO_2 (15 min), and Nd^{3+}, Yb^{3+}:CeF_3/CeO_2 (120 min) nanoparticles are presented in Fig. 2a and b, respectively. Fig. 2a and b also show the corresponding size distribution histograms.

According to the TEM imaging, the single-phase Nd^{3+}, Yb^{3+}:CeF_3 nanoparticles synthesized via the co-precipitation method (without annealing) demonstrated a relatively regular oval shape with 19 ± 2 nm average diameter (corresponding TEM image and the size distribution

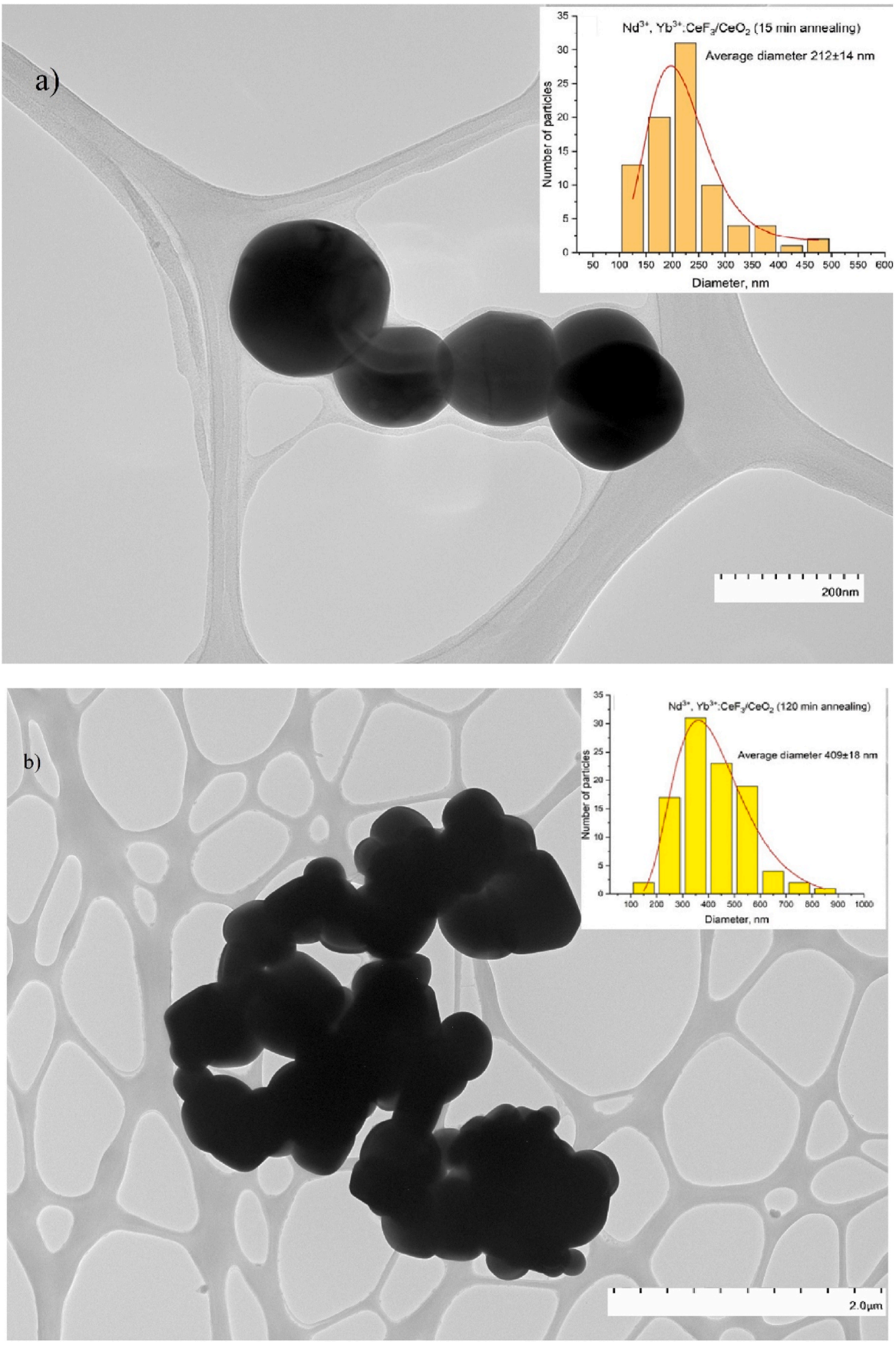

Fig. 2. TEM images of Nd^{3+}, Yb^{3+}:CeF_3/CeO_2 (15 min (a)), and Nd^{3+}, Yb^{3+}:CeF_3/CeO_2 (120 min (b)). The insets show the size distribution histograms.

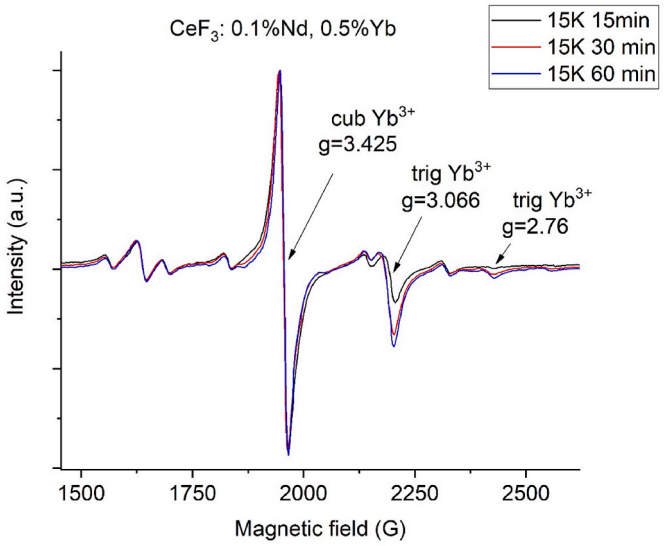

Fig. 3. EPR spectra of Nd^{3+}, Yb^{3+}:CeF_3/CeO_2 (15, 30, and 60 min) nanoparticles.

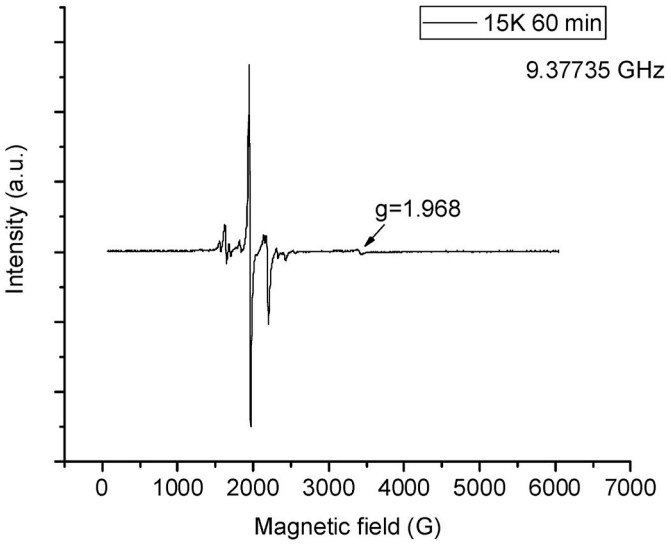

Fig. 4. Extended EPR spectrum of Nd^{3+}, Yb^{3+}:CeF_3/CeO_2 (60 min) nanoparticles.

histogram are presented in Fig. S1a of the Supplementary file). However, after 15 min of the annealing procedure, the average diameter increased to 212 ± 14 nm. We expect, that it occurs due to the sintering of the CeF_3 nanoparticles during the annealing process. Then, the average diameter increases with the increase of the annealing time. In order to conclude about the structure of the obtained composites, we analyzed the Brag peak widths at half maximum (β). It is well known, that the size of the coherent scattering domain (CSD) of a nanoparticle is inversely proportional to β (the Debye-Scherrer formula [30], equation S(1) of the Supplementary file, where β is a peak width at half of the maximum).

It can be seen, that the physical diameter increases to 212 ± 14 nm even after 15 min of the annealing. Then, it gradually increases to 409 ± 18 nm (after 120 min of annealing). It can be suggested, that the increase of the diameter is related to the increase of the efficiency of the nanoparticles sintering.

According to the analysis of the CSD diameters of both CeF_3 and CeO_2 phases, the CSD of both phases demonstrated nano-sized dimensionality several times less than the physical diameters (in the 50–70 nm range, Table S1 of the Supplementary file). Probably, the relatively huge (larger, than 200 nm) nanoparticles consist of the sintered nanosized CeF_3 and CeO_2 ones. In addition, the XRD peaks corresponding to the different *hkl* (Miller indices) have the same peak broadening. It can be suggested, that there are no directions of preferable growth of CeF_3 and CeO_2 phases and the phases of CeF_3 and CeO_2 have relatively regular shapes.

Finally, it can be suggested, that the studied Nd^{3+}, Yb^{3+}:CeF_3/CeO_2 composites are sintered Nd^{3+}, Yb^{3+}:CeF_3 and Nd^{3+}, Yb^{3+}:CeO_2 nanoparticles having relatively regular shapes and diameters of CSD around 60 nm.

3.2. EPR spectroscopy of Nd^{3+}, Yb^{3+}:CeF_3/CeO_2 nanoparticles

Fig. 3 shows experimental EPR spectra of composite Nd^{3+}, Yb^{3+}:CeF_3/CeO_2 (15, 30, and 60 min) nanoparticles.

These measurements were carried out with an X-band CW Bruker ESP300 spectrometer at a low temperature of 15 K. Because composite nanoparticles consist of two parts, paramagnetic CeF_3 and diamagnetic CeO_2, we suppose that these rather well-resolved powder spectra are due to CeO_2 part. As was shown in our recent research [31], the EPR spectrum of Er^{3+} ions, doped in CeF_3 nanoparticles, could not be observed due to the magnetic interactions between Ce^{3+} ions and doped rare-earth ions. EPR spectra look similar for all three samples and consist of the intensive line with g~3.43 surrounded by the weaker lines. The line with g~3.43 is due to even isotopes of Yb^{3+} ions in the cubic crystal field of CeO_2 structure and observed earlier in bulk crystals [32], and nanoparticles CeO_2 [33]. The less intensive lines are due to odd isotopes ^{171}Yb (with an abundance of 14.28 %, a nuclear spin of 1/2) and due to ^{173}Yb (with an abundance of 16.13 %, and a nuclear spin 5/2). The line with g~3.066 is assigned to trigonal sites, observed in bulk crystals [34,35], and in nanoparticles CeO_2 [36]. The intensity of this line increases with the increase of the annealing time, that is, the concentration of trigonal sites increases. In this case, the trigonal site is formed by substitution of one of the nearest-neighbor oxygen ions around the Yb^{3+} ion by the fluorine ion or a hydroxyl group. In case of composite Nd^{3+}, Yb^{3+}:CeF_3/CeO_2 nanoparticles the most probable substituting ion is the fluorine ion. The line with g~2.76 is assigned to the second type of trigonal sites, related to the oxygen vacancies in the nearest-neighbor environment of Yb^{3+} ion [37]. The intensity of this line also increases with increasing annealing time. This means more vacancies form with annealing time in close vicinity of Yb^{3+} ion. In contrast to the well-resolved EPR spectra of Yb^{3+} ions, the EPR lines of Nd^{3+} ions were not detected in the studied samples. EPR of Nd^{3+} ions in bulk CeO_2 crystals was observed by W.Low and S.Maniv [38], who reported a g-value of 2.415 and hyperfine structure constants of $A^{143} = 219.3$ G and $A^{145} = 136.4$ G. More detailed study of Nd^{3+} ions in bulk CeO_2 crystals was carried out by Abdulsabirov et al. [39], who found a weak splitting of the cubic line merging in one line with g = 2.422 at a trigonal orientation of the crystal. In a cubic crystal field, the lowest state of Nd^{3+} ion is a quartet Γ_8 [40], which may be the reason of the observed splitting. Fig. 4 shows extended EPR spectrum of Nd^{3+}, Yb^{3+}:CeF_3 annealed at 60 min.

It is seen in Fig. 4 a weak line with g~1.97, which can be attributed to the small number of Gd^{3+} ions. The line around g value of 2.41–4.42 was not present in the spectrum, which means an absence of Nd^{3+} cubic sites in CeO_2 nanoparticles. Authors of ref. [39] reported that no any trigonal sites of Nd^{3+} ions were observed in bulk CeO_2 crystals. This was explained by L.Y.Shekun [41], that the lowest level of Nd^{3+} ions in trigonal crystal field is non-resonating doublet $\Gamma_{4,5}$ and transition probability is zero for any orientation of magnetic fields. We suppose that in studied CeO_2 nanoparticles the doped Nd^{3+} ions are located in the trigonal crystal field, with a charge compensator situated along the local <111> axis.

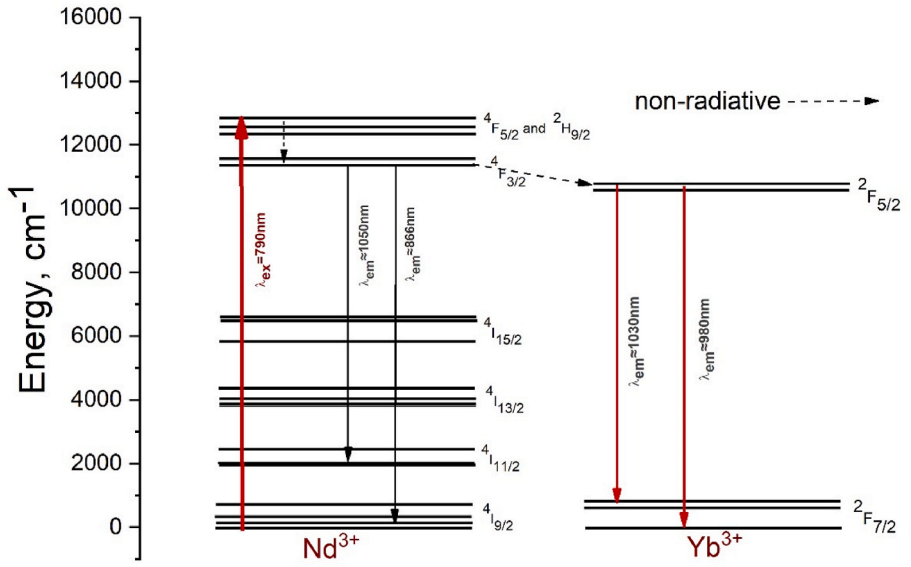

Fig. 5. Energy level diagram of Nd^{3+}/Yb^{3+} system. $\lambda_{ex} = 790$ nm corresponds to $^4I_{9/2} - {}^4F_{5/2}$ absorption band of Nd^{3+}.

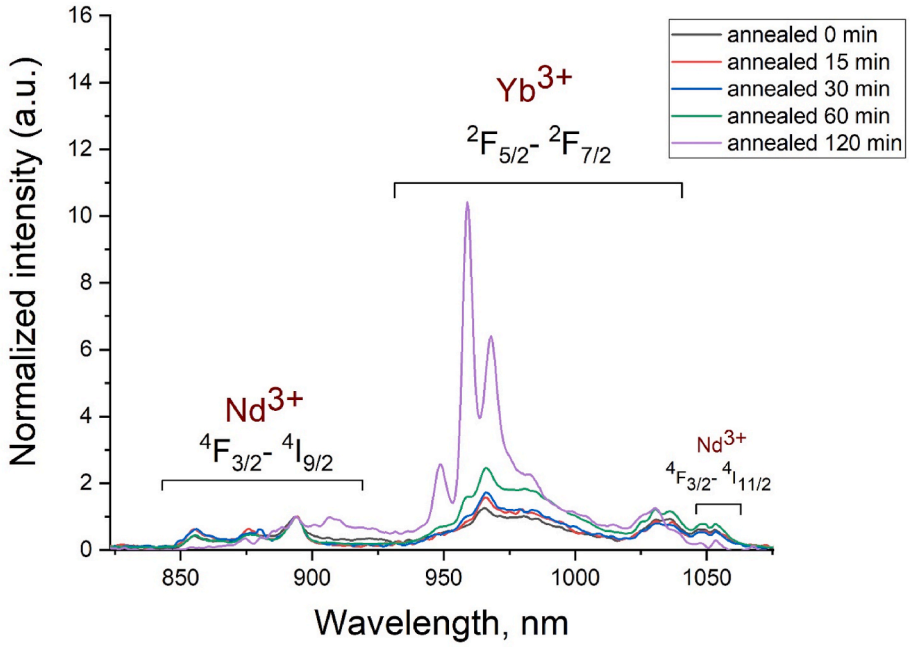

Fig. 6. Room temperature luminescence spectra of the Nd^{3+}, Yb^{3+}:CeF_3 and Nd^{3+}, Yb^{3+}:CeF_3/CeO_2 (15, 30, 60, and 120 min) nanoparticles. The 790 nm excitation wavelength corresponds to the $^4F_{5/2}$ - $^2H_{9/2}$ absorption band of Nd^{3+} ions.

3.3. Spectral characterization of the samples

Energy level diagram of Nd^{3+}/Yb^{3+} system is presented in Fig. 5. Here, the excitation wavelength $\lambda_{ex} = 790$ nm corresponds to the $^4I_{9/2} - {}^4F_{5/2}$ absorption band of Nd^{3+} ion [42]. After excitation, the $^4F_{5/2} - {}^4F_{3/2}$ non-radiative transition occurs. In addition, there are phonon-assisted $^4F_{3/2}$ (Nd^{3+}) – $^2F_{5/2}$ (Yb^{3+}) energy transfer.

Room temperature luminescence spectra of the Nd^{3+}, Yb^{3+}:CeF_3 and Nd^{3+}, Yb^{3+}:CeF_3/CeO_2 (15, 30, 60, and 120 min) nanoparticles are presented in Fig. 6. All the luminescence peaks were interpreted as Nd^{3+} ($^4F_{3/2}$ - $^4I_{9/2}$ (≈870 nm)) and $^4F_{3/2}$- $^4I_{11/2}$ (≈1050 nm) transitions, as well as Yb^{3+} ($^2F_{5/2}$ - $^2F_{7/2}$ (≈980 nm)) transition.

The presence of intense Yb^{3+} emission upon excitation of Nd^{3+} ions indicates an effective energy transfer from Nd^{3+} to Yb^{3+}. It can also be seen, that the Yb3+ peak shifts toward shorter wavelengths closer to Nd3+ peak for the single-phase Nd^{3+}, Yb^{3+}:CeF_3/CeO_2 (120 min). It indicates, that the energy gap between 4F3/2 (Nd3+) and 2F5/2 (Yb3+) is decreases compared to single-phase Nd3+, Yb3+:CeF3 sample (without annealing). Probably, this decrease in the energy gap value implements the more effective Nd3+ - Yb3+ energy transfer, and the higher Yb3+ luminescence intensity compared to Nd3+ one is clearly observed.

These energy transfer processes between Nd^{3+} and Yb^{3+} involve the $^4F_{3/2}$ (Nd^{3+}) and $^2F_{5/2}$ (Yb^{3+}) levels. In this work, the $^4F_{3/2}$ (Nd^{3+}) level is populated through multiphonon relaxation from the $^4F_{5/2}$ higher-lying energy states ($\lambda_{ex} = 790$ nm). As it was mentioned above, the back energy transfer from Yb^{3+} to Nd^{3+} is also possible. There is also energy diffusion between Yb^{3+} ions. However, this process is seemingly

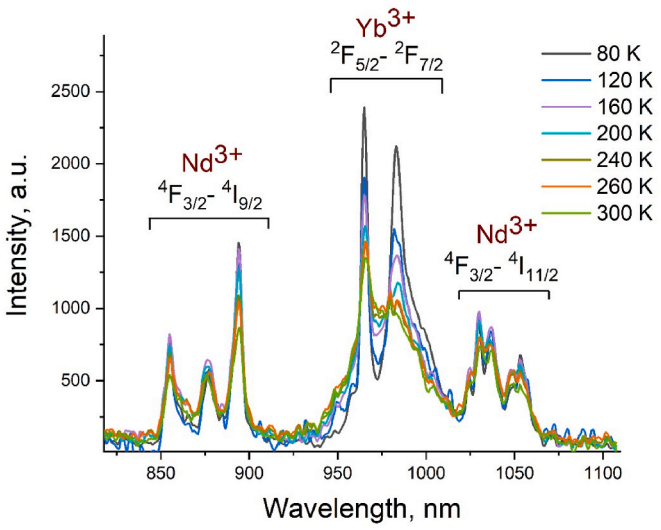

Fig. 7. The temperature evolution of the normalized luminescence spectra of Nd3+, Yb3+:CeF3 nanoparticles in the 80–320 K temperature range.

possible for the higher temperatures (above 400 K) [20]. There is also energy diffusion between Yb^{3+} ions. In the case of energy transfer between Nd^{3+} ions at 0.1 mol.% concentration, this issue is still questionable. In our previous work, we studied Nd^{3+} doped fluoride nano- and microparticles and made a suggestion, that at 0.5 mol.% of Nd^{3+}, the interaction between Nd^{3+} still occurs (via cross-relaxation) [22]. However, for 0.1 mol.% Nd^{3+} concentration the interaction is absent due to a large distance between Nd^{3+} ions, according to our conclusions. The interaction between Nd^{3+} and Yb^{3+} is dipole-dipole. The efficiency of this interaction is inversely proportional to the distance of degree six, which makes it highly sensitive to the change in the distance value. It can be seen that the intensities of both Nd^{3+} ($^4F_{3/2} - {}^4I_{9/2}$) and Yb^{3+} ($^2F_{5/2} - {}^2F_{7/2}$) luminescence peaks are interdependent due to the energy transfer processes mentioned above. Therefore, for further luminescence intensity ratio (LIR) calculations, the 848–925 nm ($^4F_{3/2} - {}^4I_{9/2}$) Nd^{3+} and 925–1048 nm ($^2F_{5/2} - {}^2F_{7/2}$) Yb^{3+} spectral ranges were chosen.

3.4. Temperature-dependent spectral-kinetic characterization of the samples

The temperature evolution of the normalized luminescence spectra of Nd3+, Yb3+:CeF3 nanoparticles in the 80–320 K temperature range is shown in Fig. 7.

The relative intensities of Nd^{3+} and Yb^{3+} emission peaks depend on temperature for all the samples. To analyze this spectral temperature dependence, LIR as a function of temperature was calculated for all the samples according to the equation:

$$LIR\ (T) = \frac{\int I_{Nd}(\lambda, T)d\lambda}{\int I_{Yb}(\lambda, T)d\lambda} \quad (1)$$

The LIR curves and fitting curves are shown in Fig. 8. It can be seen, that the shape of the LIR function depends on the phase composition of the samples as well as on the ratio of the phases.

It can be seen, that the LIR has a complex dependence on both temperature and sample's structure. Specifically, for single-phase Nd^{3+}, Yb^{3+}:CeF_3 and Nd^{3+}, Yb^{3+}:CeF_3/CeO_2 (120 min) nanoparticles, the LIR function gradually decreases and increases with temperature, respectively. In turn, the double-phase Nd^{3+}, Yb^{3+}:CeF_3/CeO_2 (15, 30, and 60 min) nanoparticles showed more complicated LIR dependencies which displayed increasing and decreasing parts of the LIR functions. It seems that the LIR functions for the Nd^{3+}, Yb^{3+}:CeF_3/CeO_2 (15, 30, and 60 min) nanoparticles are combinations of the LIR functions of single-phase samples. Thus, in order to explain all the LIR dependencies, we need to focus on the single-phase Nd^{3+}, Yb^{3+}:CeF_3 and Nd^{3+}, Yb^{3+}:CeF_3/CeO_2 (120 min) nanoparticles. To learn more about the physical background of the LIR functions, the luminescence decay curves of the Nd^{3+}, Yb^{3+}:CeF_3 and Nd^{3+}, Yb^{3+}:CeF_3/CeO_2 (120 min) nanoparticles (λ_{em} = 863 nm, $^4F_{3/2} - {}^4I_{9/2}$ transition of Nd^{3+}) were also detected (Fig. 9a and b, respectively). The rest of the decay curves are presented in Fig. S2 of the supplementary.

It can be seen, that the luminescence decay curves of Nd^{3+}, Yb^{3+}:CeF_3 nanoparticles are not perfectly single-exponential. This deviation

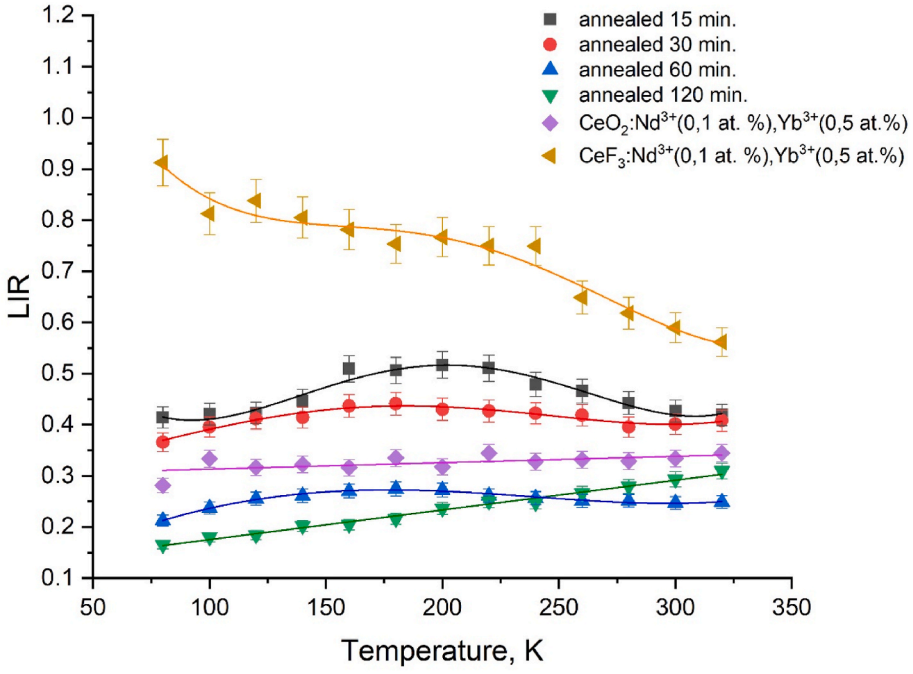

Fig. 8. Luminescence intensity ratio (LIR) dependencies on temperature. Note that the larger standard deviation values for Nd^{3+}, Yb^{3+}:CeF_3 sample can be related to the lower luminescence intensity due to different quenchers.

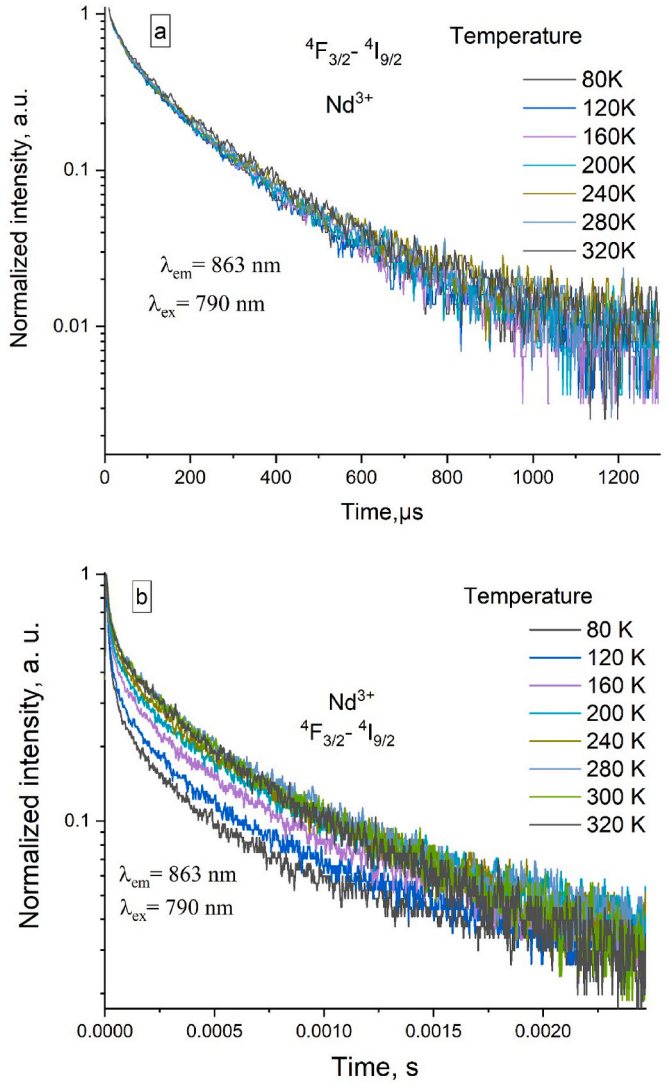

Fig. 9. Luminescence decay curves of the Nd^{3+}, Yb^{3+}:CeF_3 and Nd^{3+}, Yb^{3+}:CeF_3/CeO_2 (120 min) nanoparticles (λ_{em} = 863 nm, $^4F_{3/2}$ – $^4I_{9/2}$ transition of Nd^{3+}) in the 80–320 K temperature range. 790 nm excitation wavelength corresponds to $^4I_{9/2}$ – $^4F_{5/2}$ absorption band of Nd^{3+}.

from the single-exponential shape can be related to the different distribution of Yb^{3+} ions around Nd^{3+} ones, which results in the difference in the rate of luminescence decay of each Nd^{3+} ion. The temperature dependence of the decay curves of the Nd^{3+}, Yb^{3+}:CeF_3 nanoparticles is weak. In the case of the Nd^{3+}, Yb^{3+}:CeF_3/CeO_2 (120 min) nanoparticles, the deviation of luminescence decay curves from single-exponential function is more pronounced. The observed phenomena required more detailed research. Here, we can make a suggestion, that in the CeO_2 host, Nd^{3+} ions tend to form clusters due to the notable difference in the ionic radii of Nd^{3+} and Ce^{4+}, unlike CeF_3, where Ce^{3+} and Nd^{3+} have closer ionic radii, and the distribution of Nd^{3+}, is probably, more homogeneous. In addition, it can be suggested, that Yb^{3+} ions also form clusters in the CeO_2 host.

As it was mentioned above, the LIR function for Nd^{3+}/Yb^{3+} - doped CeF_3 nanoparticles is a decay function. This phenomenon can be explained by the fact that the energy transfer efficiency from Nd^{3+} to Yb^{3+} increases with the increase of temperature. Hence, the intensity of Nd^{3+} lowers while the intensity of Yb^{3+} increases. Thus, LIR function (I_{Nd}/I_{Yb}) is a decay function. The LIR function of the Nd^{3+}, Yb^{3+}:CeF_3/CeO_2 (120 min) nanoparticles is an increasing function. The physical background of the LIR function is more complicated due to the ion clustering, suggestively. There are the same energy transfer processes when Nd^{3+} transmits the excitation energy to Yb^{3+}, and the efficiency of this transition increases with the temperature increase. However, here, the Yb^{3+} intensity is quenched due to the concentration quenching, which is more effective in clusters. Finally, the intensity of Nd^{3+} decrease due to the energy transfer to Yb^{3+}. In turn, Yb^{3+} intensity decreases more sharply due to the effective concentration quenching in the Yb^{3+} clusters. In addition, according to the EPR data, there are Yb^{3+} trigonal centers formed by OH groups and oxygen vacancies. These kinds of impurities can also serve as temperature-dependent quenchers of Yb^{3+} emission. Here, the LIR is the ratio of two decreasing functions ($I_{Nd}(T)/I(_{Yb}(T))$ where the consequent ($I_{Yb}(T)$) decreases faster. Note, that we do not show the values of intensity of both ions as functions of temperature. The reason that we do not consider these parameters is that the luminescence intensity strongly depends on the intensity of the excitation irradiation. Even the small fluctuations of the excitation intensity affect the luminescence intensity of the ions. The precise measurements of intensity as function of temperature require additional procedures of calibration and, probably, the use of an integrating sphere. Such measurements is the next step of the present work. The presence of Yb^{3+} clusters is intermediately confirmed by the above-mentioned EPR data. Indeed, it was established, that there are several types of trigonal centers.

In order to compare the temperature behavior of Nd^{3+}/Yb^{3+} ion pair, we conducted spectral characterization of Nd^{3+}/Yb^{3+} - doped CeO_2 nanoparticles obtained via chemical rout. The Nd^{3+}/Yb^{3+} - doped CeO_2 obtained via chemical rout nanoparticles demonstrated the same increasing character of the LIR function probably, due to similar physical mechanism.

Now it is difficult to make a correct approximation function for the obtained LIR dependencies. In order to establish the physical mechanism of temperature sensitivity, the additional experiments with different concentration of the doping ions are required. To obtain such important performances as absolute (S_a) and relative (S_r) temperature sensitivities, we approximated the LIR dependencies via polynomial functions [1,3].

$$S_a = \left|\frac{dLIR}{dT}\right|, \tag{2}$$

$$S_r = \frac{1}{LIR}\left|\frac{dLIR}{dT}\right| \cdot 100\%, \tag{3}$$

where S_a is defined as the change in the LIR function with a temperature change of 1 K, and S_r is the percentage change in the value of the LIR function relative to itself with a temperature change of 1 K. The S_a and S_r curves for samples at different annealing times are shown in Fig. 10a and b, respectively.

The obtained parameters are compared with the analogs operating in the “biological window” are compared in Table 1.

It is seen, that the studied samples demonstrate very competitive performances. There are some systems, which show higher sensitivities. On the other hand, the absolute and relative temperature sensitivities are not comprehensive characteristics of the luminescence temperature sensors. According to the above-mentioned sources, both CeO_2 and CeF_3 compounds showed low cytotoxicity, which is very important for the safety of the personnel. In turn, many compounds listed in Table 1 were not studied in terms of biological activity. In addition, both doped single-phase CeO_2 and CeF_3 samples demonstrated increasing and decreasing character of LIR function respectively, without extremums in the whole 80–320 K temperature range. For such dependencies, one particular LIR value corresponds to one temperature value.

4. Conclusions

Here we synthesized single-phase (hexagonal structure) Nd^{3+}, Yb^{3+}:CeF_3 nanoparticles via the co-precipitation method. These nanoparticles

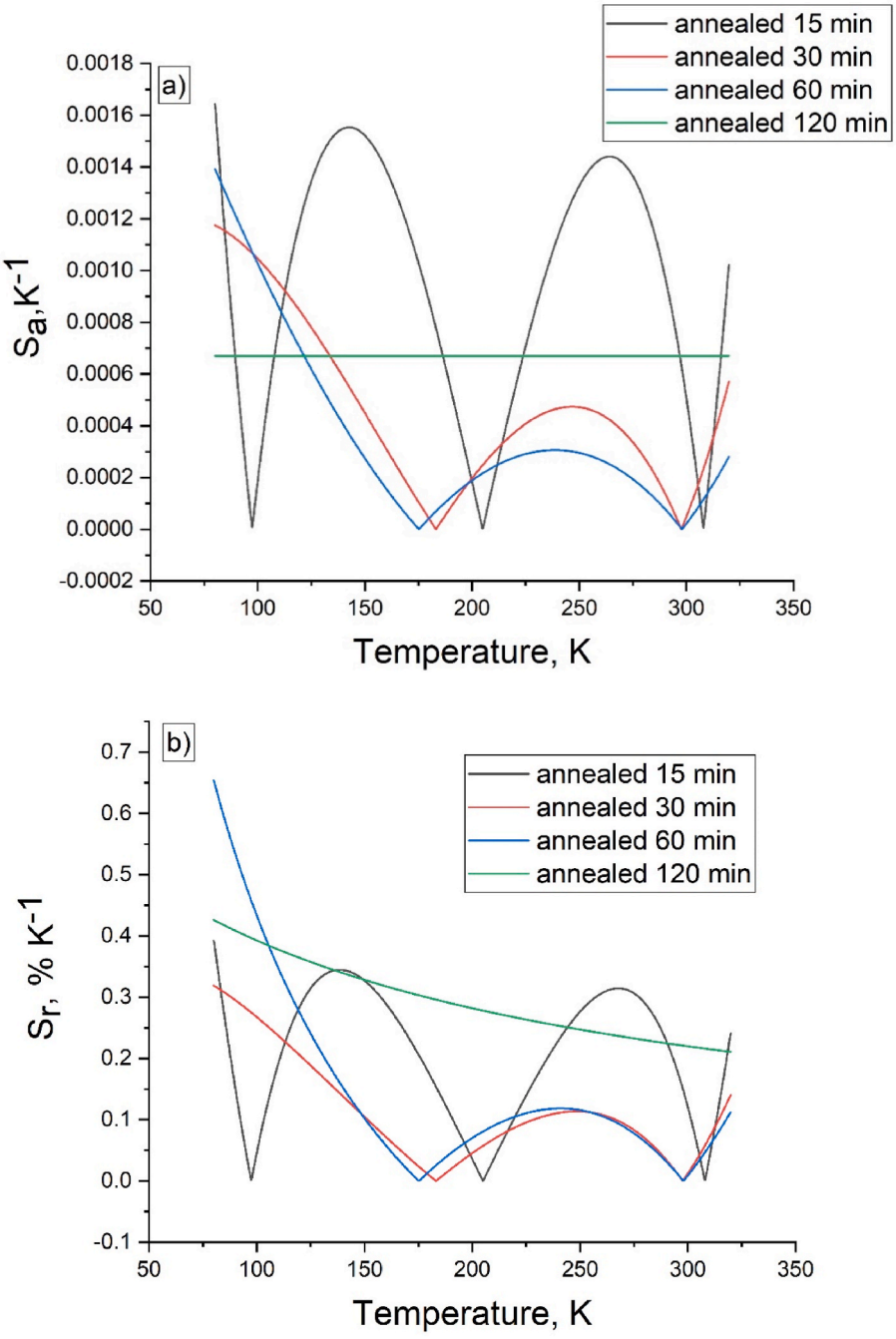

Fig. 10. Absolute S_a (a) and relative S_r (b) temperature sensitivities of the samples.

Table 1
The comparison of the performances of luminescence sensors.

Sample	Transitions, Detected Wavelengths, and Conditions of the Excitation	Maximum S_a [K^{-1}]	Maximum S_r [%·K^{-1}]	T,K	Ref.
LSG: 0.04Nd^{3+}, 0.05 Yb^{3+}	$^2F_{5/2} \rightarrow {}^2F_{7/2}$ (Yb^{3+})/$^4F_{3/2} \rightarrow {}^4I_{11/2}$ (Nd^{3+})	0.0069708	0.49	303K	[43]
YAG: Yb^{3+}/Nd^{3+}	$^4F_{7/2}/{}^4F_{5/2} \rightarrow {}^4I_{9/2}$	0.00234 (738 K)	0.461	348–1273 K	[44]
YF_3: Tm^{3+}/Yb^{3+}	Tm^{3+}: $^3F_{2,\ 3} \rightarrow {}^3H_6$	–	0.10	300	[45]
Tm^{3+}:$LiY_{0.8}Yb_{0.2}F_4$	Tm^{3+} ($^3H_4$ – $^3H_6$)/Yb^{3+} ($^2F_{5/2}$ – $^2F_{7/2}$)	–	0.36	254–290	[46]
YF_3: Nd^{3+}/Yb^{3+}	Nd^{3+} ($^4F_{3/2}$– $^4I_{9/2}$)/Yb^{3+} ($^2F_{5/2}$– $^2F_{7/2}$)	–	0.1–0.4	80–320 K	[47]
YVO_4: Yb^{3+}/Tm^{3+}	$^3F_{2,3} \rightarrow {}^3H_6/{}^3H_4 \rightarrow {}^3H_6$	–	0.25	300	[48]
$LiNbO_3$:Yb^{3+}/Tm^{3+}	$^3F_{2,3} \rightarrow {}^3H_6$, $^1G_4 \rightarrow {}^3F_4$ ($^5F_4/{}^5S_2$), $^5F_5 \rightarrow {}^5I_8$	0.00024	0.35	323–773	[49]
$ZnWO_4$: Tm^{3+}/Yb^{3+}/Mg^{2+}	Tm^{3+}: $^1G_4$(a) $\rightarrow {}^3H_6$ $^1G_4$(b)$\rightarrow {}^3H_6$	–	0.34	300	[50]
CeO_2:Nd^{3+}/Yb^{3+}			0.43–0.22	80–320	This work

were annealed in air at 600 °C for 15, 30, 60, and 120 min to obtain double-phase Nd^{3+}, Yb^{3+}:CeF_3/CeO_2 nanoparticles. Here, after 120 min of annealing, the single-phase Nd^{3+}/Yb^{3+}-doped cerium oxide nanoparticles were obtained (cubic phase). The Nd^{3+}, Yb^{3+}:CeF_3/CeO_2 (15, 30, and 60 min) nanoparticles demonstrated combinations of CeF_3 and CeO_2 phases. The physical size of the samples gradually increased from 19 nm (Nd^{3+}, Yb^{3+}:CeF_3) to ~ 409 nm (Nd^{3+}, Yb^{3+}:CeF_3/CeO_2 (120 min)). We made a suggestion, that the double-phase samples consist of sintered doped CeF_3 and CeO_2 nanoparticles having an average size of CSD around 65 nm. The single-phase CeO_2 sample also consists of sintered ~65 nm CeO_2 nanoparticles. We carried out spectral-kinetic characterization of the samples in the 80–320 K temperature range. The luminescence intensity ratio (LIR) was taken as a temperature-dependent parameter (LIR = I_{Nd}/I_{Yb}, where 848–925 nm ($^4F_{3/2}$ – $^4I_{9/2}$) Nd^{3+} and 925–1048 nm ($^2F_{5/2}$ – $^2F_{7/2}$) Yb^{3+}). The LIR for single-phase doped CeF_3 nanoparticles is a decreasing function in the whole 80–320 K range. In turn, for single-phase Nd^{3+}, Yb^{3+}:CeF_3/CeO_2 (120 min) nanoparticles, is an increasing function. The LIRs for double-phase samples are more complicated and can be considered as a combination of LIRs of single-phase CeF_3 and CeO_2 samples. The decreasing character of the LIR function was explained by the fact, that Nd^{3+} transfers the energy to Yb^{3+} via phonon-assisted energy transfer which is more effective at higher temperatures. Here, the Nd^{3+} intensity decreases while Yb^{3+} one increases with the temperature increase. Thus, the I_{Nd}/I_{Yb} (T) is a decreasing function. For Nd^{3+}, Yb^{3+}:CeF_3/CeO_2 (120 min) nanoparticles, Nd^{3+} luminescence decay curves are significantly non-exponential. It was suggested, that such behavior is related to the fact, that the trivalent doping ions form clusters in the CeO_2 host. Seemingly, these clusters are different between each other. In such clusters, the concentration quenching of Yb^{3+} occurs more effectively. Finally, the Nd^{3+} intensity decreases via energy transfer to Yb^{3+}. In turn, Yb^{3+} is quenched by the concentration quenching and decreases more sharply. Probably, these processes provide an increasing character of doped CeO_2 LIR function. In addition, we chemically synthesized Nd^{3+}/Yb^{3+} doped CeO_2 nanoparticles as physically characterized them. They showed similar LIR dependency.

The maximal relative temperature of Nd^{3+}/Yb^{3+} doped CeO_2 sample (annealed for 120 min) is around 0.2 %/K, which is a very competitive value. The most important thing, is that here, the LIR function allows uniquely identifying the temperature at least in the studied broad temperature range. The ability to operate in the biological window and low toxicity of CeF_3 and CeO_2 makes the nanoparticles possible to be utilized for biomedical applications.

CRediT authorship contribution statement

A.K Ginkel: Writing – review & editing, Methodology, Investigation, Formal analysis, Data curation. **R.M Rakhmatullin:** Writing – review & editing, Writing – original draft, Methodology, Investigation, Formal analysis, Conceptualization. **O.A Morozov:** Methodology, Investigation, Data curation. **I.A Zagrai:** Investigation, Data curation. **S.L Korableva:** Methodology, Investigation. **M.S Pudovkin:** Writing – original draft, Project administration, Investigation, Funding acquisition, Data curation, Conceptualization.

Funding

The research was funded by the subsidy allocated to Kazan Federal University for the state assignment in the sphere of scientific activities (FZSM-2022-0021).

Declaration of competing interest

The authors declare that they have no known competing financial interests or personal relationships that could have appeared to influence the work reported in this paper.

Appendix A. Supplementary data

Supplementary data to this article can be found online at https://doi.org/10.1016/j.optmat.2024.116580.

Data availability

Data will be made available on request.

References

[1] C.D.S. Brites, et al., Spotlight on luminescence thermometry: basics, challenges, and cutting-edge applications, Adv. Mater. 35 (36) (Sep. 2023), https://doi.org/10.1002/adma.202302749.
[2] L. Đačanin Far, M.D. Dramićanin, Luminescence Thermometry with Nanoparticles: A Review, Multidisciplinary Digital Publishing Institute (MDPI), Nov. 01, 2023, https://doi.org/10.3390/nano13212904.
[3] E.P. Santos, et al., Towards accurate real-time luminescence thermometry: an automated machine learning approach, Sens. Actuators A Phys. 362 (Nov. 2023), https://doi.org/10.1016/j.sna.2023.114666.
[4] L. Marciniak, K. Kniec, K. Elżbieciak-Piecka, K. Trejgis, J. Stefanska, M. Dramićanin, Luminescence Thermometry with Transition Metal Ions. A Review, Elsevier B.V., Oct. 15, 2022, https://doi.org/10.1016/j.ccr.2022.214671.
[5] M.D. Dramićanin, Trends in Luminescence Thermometry, American Institute of Physics Inc, Jul. 28, 2020, https://doi.org/10.1063/5.0014825.
[6] N. Jurga, M. Runowski, T. Grzyb, Lanthanide-based nanothermometers for bioapplications: excitation and temperature sensing in optical transparency windows, J. Mater. Chem. C Mater. 12 (32) (2024) 12218–12248, https://doi.org/10.1039/D3TC04716D.
[7] A. Yakovliev, et al., Noninvasive temperature measurement in dental materials using Nd3+, Yb3+ doped nanoparticles emitting in the near infrared region, Part. Part. Syst. Char. 37 (2) (2020) 1–8, https://doi.org/10.1002/ppsc.201900445.
[8] Y. Chen, et al., Real-time ratiometric optical nanoscale thermometry, ACS Nano 17 (3) (Feb. 2023) 2725–2736, https://doi.org/10.1021/acsnano.2c10974.
[9] R. Piñol, C.D.S. Brites, N.J. Silva, L.D. Carlos, A. Millán, Nanoscale Thermometry for Hyperthermia Applications, 2018, https://doi.org/10.1016/B978-0-12-813928-8.00006-5.
[10] N.R. Datta, et al., Local hyperthermia combined with radiotherapy and-/or chemotherapy: recent advances and promises for the future, Cancer Treat Rev. 41 (9) (2015) 742–753, https://doi.org/10.1016/j.ctrv.2015.05.009.
[11] P.P. Fedorov, A.A. Luginina, S.V. Kuznetsov, V.V. Osiko, Nanofluorides, J. Fluor. Chem. 132 (12) (2011) 1012–1039, https://doi.org/10.1016/j.jfluchem.2011.06.025.
[12] P.P. Fedorov, V.V. Semashko, S.L. Korableva, Lithium rare-earth fluorides as photonic materials: 1. Physicochemical characterization, Inorg. Mater. 58 (3) (2022) 223–245, https://doi.org/10.1134/S0020168522030049.
[13] M.S. Pudovkin, et al., Toxicity of laser irradiated photoactive fluoride PrF3 nanoparticles toward bacteria, J. Phys. Conf. Ser. 560 (1) (2014), https://doi.org/10.1088/1742-6596/560/1/012011.
[14] M.S. Pudovkin, et al., Photoinduced toxicity of PrF3 and LaF3 nanoparticles, Optics Spectrosc. (English translation of Optika i Spektroskopiya) 121 (4) (2016) 538–543, https://doi.org/10.1134/S0030400X16100209.
[15] M.S. Pudovkin, P.V. Zelenikhin, V.V. Shtyreva, V.G. Evtugyn, V.V. Salnikov, A. S. Nizamutdinov, V.V. Semashko, Cellular uptake and cytotoxicity of unmodified Pr3+: LaF3 nanoparticles, J. Nanoparticle Res. 21 (2019) 1–13.
[16] L. Marciniak, A. Bednarkiewicz, K. Elzbieciak, NIR-NIR photon avalanche based luminescent thermometry with Nd3+ doped nanoparticles, J. Mater. Chem. C Mater. 6 (28) (2018) 7568–7575, https://doi.org/10.1039/c8tc01553h.
[17] B. Del Rosal, et al., Neodymium-doped nanoparticles for infrared fluorescence bioimaging: the role of the host, J. Appl. Phys. 118 (14) (2015), https://doi.org/10.1063/1.4932669.
[18] C. Jacinto, et al., Subtissue thermal sensing based on neodymium-doped LaF3 nanoparticles, ACS Nano 7 (2) (2013) 1188–1199.
[19] F.B. Costa, et al., High Nd3+→Yb3+ energy transfer efficiency in tungsten-tellurite glass: a promising converter for solar cells, J. Am. Ceram. Soc. 100 (5) (2017) 1956–1962, https://doi.org/10.1111/jace.14770.
[20] L. Marciniak, A. Bednarkiewicz, M. Stefanski, R. Tomala, D. Hreniak, W. Strek, Near infrared absorbing near infrared emitting highly-sensitive luminescent nanothermometer based on Nd3+ to Yb3+ energy transfer, Phys. Chem. Chem. Phys. 17 (37) (2015) 24315–24321, https://doi.org/10.1039/c5cp03861h.
[21] X. Bian, et al., Near-infrared luminescence and energy transfer mechanism in K2YF5:Nd3+, Yb3+, Mater. Res. Bull. 110 (August 2018) (2019) 102–106, https://doi.org/10.1016/j.materresbull.2018.10.024.
[22] M. Pudovkin, E. Oleynikova, A. Kiiamov, M. Cherosov, M. Gafurov, Nd3+, Yb3+: YF3 optical temperature nanosensors operating in the biological windows, Materials 16 (1) (2022) 39.
[23] A.B. Shcherbakov, N.M. Zholobak, A.E. Baranchikov, A.V. Ryabova, V.K. Ivanov, Cerium fluoride nanoparticles protect cells against oxidative stress, Mater. Sci. Eng. C 50 (2015) 151–159, https://doi.org/10.1016/j.msec.2015.01.094.
[24] A. Trovarelli, Catalytic properties of ceria and CeO2-Containing materials, Catal. Rev. Sci. Eng. 38 (4) (1996) 439–520, https://doi.org/10.1080/01614949608006464.

[25] E.M. Alakshin, et al., Microwave-assisted hydrothermal synthesis and annealing of DyF3 nanoparticles, J. Nanomater. 2016 (3) (2016) 1–6, https://doi.org/10.1155/2016/7148307.
[26] O.S. Polezhaeva, N.V. Yaroshinskaya, V.K. Ivanov, Formation mechanism of nanocrystalline ceria in aqueous solutions of cerium (III) nitrate and hexamethylenetetramine, Inorg. Mater. 44 (2008) 51–57.
[27] V.K. Ivanov, O.S. Polezhaeva, YuD. Tretyakov, Nanocrystalline cerium dioxide: synthesis, structure-sensitive properties and promising areas of application, Russ. Chem. J. 53 (2) (2009) 56–67.
[28] C. Sun, H. Li, L. Chen, Nanostructured ceria-based materials: synthesis, properties, and applications, Energy Environ. Sci. 5 (9) (2012) 8475–8505, https://doi.org/10.1039/c2ee22310d.
[29] G. Wang, Q. Peng, Y. Li, Lanthanide-doped nanocrystals: synthesis, optical-magnetic properties, and applications 44 (5) (2011).
[30] M.S. Pudovkin, et al., Luminescence Nanothermometry Based on Pr3+: LaF3 Single Core and Pr3+:LaF3/LaF3 Core/Shell Nanoparticles, vol. 2019, 2019.
[31] M.S. Pudovkin, et al., EPR and optical study of erbium-doped CeO2 and CeO2/CeF3 nanoparticles, Ceram. Int. 50 (6) (Mar. 2024) 9263–9269, https://doi.org/10.1016/j.ceramint.2023.12.242.
[32] Y. Komet, W. Low, R.C. Linares, Paramagnetic resonance of rare earth ions in cerium oxide, Phys. Lett. 19 (1965) 473–474, https://doi.org/10.1016/0031-9163(65)90108-3.
[33] R.M. Rakhmatullin, V.V. Pavlov, V.V. Semashko, S.L. Korableva, Room-temperature ferromagnetism in cerium dioxide powders, J. Exp. Theor. Phys. 121 (2) (Aug. 2015) 274–278, https://doi.org/10.1134/S1063776115080221.
[34] A.A. Antipin, Z.N. Zonn, V.A. Ioffe, A.N. Katyshev, L.Y. Shekun, Trivalent rare earths in single crystals of cerium dioxide. Erbium and ytterbium. Sov, Phys. Solid State 9 (1967) 521–522.
[35] M.J.M. Baker, T.Rs Reddy, R.L. Wood, ENDOR of trigonal sites of Yb^{3+} in CeO_2 and ThO_2, J. Phys. C Solid State Phys. 12 (1979) 3317, https://doi.org/10.1088/0022-3719/12/16/019.
[36] R.M. Rakhmatullin, O.A. Morozov, S.L. Korableva, A.A. Rodionov, Oxygen vacancies, hydroxyl groups and fluorine ions in the local environment of Yb3+ ions doped in CeO2 nanoparticles, Ceram. Int, Sep. (2024), https://doi.org/10.1016/j.ceramint.2024.09.003.
[37] M.M. Abraham, R.A. Weeks, G.W. Clark, C.B. Finch, Electron spin resonance of rare-earth ions in CeO_2: Yb^{3+} and Er^{3+}, Phys. Rev. 148 (1966) 350–352, https://doi.org/10.1103/PhysRev.148.350.
[38] W. Low, S. Maniv, ESR spectra of Nd^{3+}, Er^{3+}, Yb^{3+}, and Gd^{3+} in single crystals of CeO_2, Bull. Am. Phys. Soc. 12 (1967) 641.
[39] [a] J R.Yu Abdulsabirov, Z.N. Zonn, A.N. Katyshev, Kristallografia, vol. 14, 1969, pp. 919–920 (in Russian);
[b] R.Yu Abdulsabirov, Z.N. Zonn, A.N. Katyshev, Investigation of EPR of Nd^{3+} in CeO_2 monocrystals, Sov. Phys. Crystallogr. 14 (1970) 793.
[40] M. J. Weber and R. W. Bierig, "Paramagnetic Resonance and Relaxation of Trivalent Rare-Earth Ions in Calcium Fluoride. I. Resonance Spectra and Crystal Fields.".
[41] L.Y. Shekun, Features of magnetic properties of trigonal and tetragonal rare earth centers in CaF2 type crystals, Fiz. Tverd. Tela 9 (1967) 948 [(Sov. Phys. Sol. State, 9, 742 (1967)).
[42] S. Balabhadra, et al., Boosting the sensitivity of Nd3+-based luminescent nanothermometers, Nanoscale 7 (41) (2015) 17261–17267, https://doi.org/10.1039/c5nr05631d.
[43] Z. Xing, et al., A perovskite-like LaSrGaO4:Mn2+, Nd3+, Yb3+ NIR luminescent material for fluorescent temperature sensor, J. Lumin. 225 (Sep) (2020), https://doi.org/10.1016/j.jlumin.2020.117352.
[44] K. Zhu, et al., Optical temperature sensing characteristics of Yb3+/Nd3+ co-doped YAG single crystal fiber based on up-conversion luminescence, J. Lumin. 267 (Mar) (2024), https://doi.org/10.1016/j.jlumin.2023.120347.
[45] H. Suo, et al., All-in-one thermometer-heater up-converting platform YF3:Yb3+, Tm3+ operating in the first biological window, J. Mater. Chem. C Mater. 5 (6) (2017) 1501–1507, https://doi.org/10.1039/c6tc05449h.
[46] A.R. Khadiev, et al., Down-conversion based Tm3+:LiY1-XYbXF4 temperature sensors, Opt. Mater. 134 (Dec) (2022), https://doi.org/10.1016/j.optmat.2022.113118.
[47] M.S. Pudovkin, A.K. Ginkel, E.V. Lukinova, Temperature sensitivity of Nd3+, Yb3+:YF3 ratiometric luminescent thermometers at different Yb3+ concentration, Opt. Mater. 119 (June) (2021) 111328, https://doi.org/10.1016/j.optmat.2021.111328.
[48] M. Runowski, P. Wozny, N. Stopikowska, I.R. Martín, V. Lavín, S. Lis, Luminescent nanothermometer operating at very high temperature-sensing up to 1000 K with upconverting nanoparticles (Yb3+/Tm3+), ACS Appl. Mater. Interfaces 12 (39) (Sep. 2020) 43933–43941, https://doi.org/10.1021/acsami.0c13011.
[49] L. Xing, W. Yang, D. Ma, R. Wang, Effect of crystallinity on the optical thermometry sensitivity of Tm3+/Yb3+ codoped LiNbO3 crystal, Sensor. Actuator. B Chem. 221 (Dec. 2015) 458–462, https://doi.org/10.1016/j.snb.2015.06.132.
[50] W. Xu, L. Zhao, F. Shang, L. Zheng, Z. Zhang, Modulating the thermally coupled status of energy levels in rare earth ions for sensitive optical temperature sensing, J. Lumin. 249 (Sep) (2022), https://doi.org/10.1016/j.jlumin.2022.119042.